CTRC Research Publications   Cooling Technologies Research Center

2020

Two-phase Flow Morphology and Local Wall Temperatures in High-Aspect-Ratio Manifold Microchannels

K. P. Drummond

J. A. Weibel

S V. Garimella

Two-Phase Flow Morphology and Local Wall Temperatures in High-Aspect-Ratio Manifold Microchannels

Kevin P. Drummond, Justin A. Weibel, Suresh V. Garimella [1]

Cooling Technologies Research Center, School of Mechanical Engineering,

and Birck Nanotechnology Center

Purdue University, West Lafayette, Indiana 47907 USA

Abstract: Manifold microchannel heat sinks can dissipate high heat fluxes at moderate pressure drops, especially during two-phase operation. High-aspect-ratio microchannels afford a large enhancement in heat transfer area; however, the flow morphology in manifold microchannels during two-phase operation, as well as the resulting thermal performance, are not well understood. In this work, a single manifold microchannel representing a repeating unit in a heat sink is fabricated in silicon with a bonded glass viewing window. Samples of different channel lengths (750 μm and 1500 μm) and depths (125 μm, 250 μm, and 1000 μm) are considered; channel and fin widths are both maintained at 60 μm. Subcooled fluid (HFE-7100) is delivered to the channel at a constant flow rate such that the fluid velocity at the inlet is ~1.05 m/s in all cases. A high-speed camera is used to visualize the two-phase flow in the channel through the glass sidewall; an infrared camera measures the temperature distribution on the opposite channel sidewall. The flow

---

[1] Corresponding author: sureshg@purdue.edu; currently President, University of Vermont

visualizations reveal that vapor nucleation occurs at stagnation regions below the manifold near the inlet plenum and at both corners adjacent to the channel base. For deep channels (1000 μm), at sufficiently high heat fluxes, vapor completely covers the base of the channels and liquid does not re-wet the surface in this region. This newly identified vapor blanketing phenomenon causes a significant decrease in performance and an increase in the measured channel wall temperatures. This study reveals the critical role of the two-phase flow morphology in manifold microchannel heat sink design.

Keywords: flow boiling; two-phase flow visualization; manifold microchannel heat sink; high aspect ratio microchannels; HFE-7100

Highlights:

- Characterization of two-phase flow through a single manifold microchannel

- Test device that mimics the heating conditions and fin effects present in high-aspect-ratio microchannels

- Flow visualizations and spatially resolved temperature measurements along the channel depth

- Evaluation of the effects of channel aspect ratio and flow length on two-phase morphology

- Observation of a vapor blanket at the bottom of deep, short flow channels that governs thermal performance

Nomenclature

A	area		*Greek symbols*	
AR	aspect ratio, $AR = d_c/w_c$		ρ	mass density
d	depth		φ	phase
D_H	hydraulic diameter		*Subscripts*	
c_p	specific heat		*avg*	average
G	mass flux, $G = \dot{m}/(w_c d_c)$		*base*	base of channels
h_{wet}	heat transfer coefficient		*c*	channel
h_{LV}	latent heat of vaporization		*f*	fin
I	electrical current		*fl*	fluid
k	thermal conductivity		*in*	inlet
L	length		*m*	manifold
L_{nd}	nondimensional length, $L_{nd} = L_c/d_c$		*out*	outlet
$\dot{m}$	mass flow rate		*sat*	saturation
q''	heat flux		*Si*	silicon
T	temperature		*tot*	total
w	width		*wet*	wetted area
z	location along channel			

1. Introduction

Next-generation radar, power electronics, and high-performance computing systems require heat sinks that can remove heat fluxes in excess of 1,000 W/cm² over the entire chip while maintaining device temperatures near their current levels [1,2]. Traditional 'remote' cooling systems utilize heat sinks that are attached to the heat-generating device, often with an intermediate heat spreader, using thermal interface materials at the mating surfaces; the temperature rise across these stacks is prohibitive at very high heat fluxes due to the long conduction paths and large temperature jumps at the interfaces. By fabricating the heat sink directly within the heat-generating device, 'embedded' cooling systems inherently avoid the parasitic thermal resistances that are characteristic of remote cooling systems. However, when the heat sink is in close proximity to the heat source, the opportunity for heat spreading is severely diminished. This exposes the heat sink directly to the high heat fluxes generated from the device and necessitates either higher heat transfer coefficients or increased heat transfer area (while maintaining the footprint area) to maintain the desired low thermal resistance across the heat sink.

Manifold microchannel heat sinks decouple fluid flow length and total heat sink size by delivering fluid to a bank of microchannels at multiple locations along the flow length. In traditional microchannel heat sinks, fluid is delivered to the channels on one end of the heat sink, flows across the entire length of the heat sink, and exits on the opposite end. Manifold microchannel heat sinks, on the other hand, provide multiple inlets and outlets along the flow length using a manifold distributor. The distance between adjacent inlet and outlet locations determines the effective flow length, instead of the length along the total heat rejection area. The pressure drop can be significantly reduced at a given mass flux in this configuration due to the

4

decrease in channel flow length. Numerical studies have predicted, and experimental studies have verified, that the total heat removal in manifold microchannel heat sinks can be significantly enhanced compared to traditional heat sinks for a given pressure drop and chip temperature during single-phase operation [3-6].

To increase the heat transfer area of a heat sink, channel width can be decreased and channel depth increased. In traditional microchannel heat sinks, diminishing returns are achieved in terms of a decrease in base temperature with increasing channel depth for high-aspect-ratio microchannels. Beyond a point, any further increase in channel depth does not result in a commensurate reduction in base temperature due to the reduction in fin efficiency [7,8]. In manifold microchannel (MMC) heat sinks, increasing channel depth beyond some threshold may even lead to base temperature increases at high aspect ratios. This has been studied for single-phase operation where optimal channel heights balance the added heat transfer area with the decreased impingement effects with increasing channel depth. Many numerical studies have identified optimized geometries for both the fluid distribution manifold and the microchannel heat sink in single-phase operation [3,4,9-17].

While single-phase performance in manifold microchannels can be predicted using numerical models and has been measured experimentally, two-phase performance has not been thoroughly studied. Baummer *et al.* [5] demonstrated dissipation of a heat flux of 300 W/cm² over a 1 cm² area using a manifold microchannel heat sink having 42 μm wide and 483 μm deep channels using HFE-7100 as the working fluid. In recent work by the authors [18,19], hierarchical manifold microchannel heat sinks were experimentally tested during two-phase operation using HFE-7100 as the working fluid. Using banks of high-aspect-ratio microchannels with depths

between 150 μm and 470 μm and widths between 15 μm and 35 μm, heat fluxes up to 1020 W/cm² were dissipated over a 5 mm × 5 mm area at chip temperatures less than 69 °C above the fluid inlet temperature and pressure drops less than 120 kPa. For the range of channel geometries tested, chip temperature decreased with increasing channel depth due to the increase in wetted area for a fixed heat flux, channel mass flux, and channel width. For small-width, high-aspect-ratio microchannels, fin efficiencies less than 50% were calculated, signifying the decrease in the performance of the added height as fins are made thinner and taller.

Flow visualizations in traditional microchannels have provided key insights into the morphological changes that occur with different channel geometries, fluid properties, flow rates, and heat fluxes [20]. Due to drastic changes in the flow morphology with each of these variables, it is difficult to generally predict performance in two-phase microchannel heat sinks with high accuracy. Rather, flow regime maps categorize discrete regions of similar flow morphology. Depending on the channel geometry and flow characteristics, flow regimes present in microchannel systems typically include bubbly, slug, and annular flows. Inside each regime, mechanistic models specific to the flow morphology yield improved predictive capabilities [21].

Flow visualizations in microchannels are used to monitor the transitions between flow regimes [22-26], measure film thicknesses [21,27], determine nucleation sites and location of the boiling front [28-30], and match transient thermal data with flow characteristics [31,32]. The data collected in these studies provide vital information necessary to develop models used to predict system performance. However, flow visualizations of two-phase flows in manifold microchannels have not been widely reported. Cetegen [33] provided flow visualizations in a single manifold microchannel unit cell with a channel length of 3.875 mm, a channel height of 2.42 mm, and

channel widths of 70 μm and 225 μm, using HFE-7100 as the working fluid. A heated copper block was used to provide a uniform wall heat flux boundary condition at the channel wall and a glass plate for optical access from the other side. For the range of mass fluxes and heat fluxes tested, flow regimes similar to traditional microchannels of the same dimensions were observed; however, vapor was sometimes trapped in the stagnation regions for certain operating conditions. Flow instabilities were also observed, which were attributed to nucleation suppression in the impingement region and vapor blockage at the outlet. Subsequent investigations by Deisenroth *et al.* [34, 35], which used the same test section as Cetegen [33], further investigated the flow boiling regimes and wall temperature maps resulting from uniform sidewall heating of a U-bend channel and noted differences in the flow phenomena compared to traditional flow regimes observed in straight microchannels.

An investigation into the two-phase flow morphology of manifold microchannels that fully represents the heating condition present in high-aspect-ratio microchannels (*viz.*, heat transfer to the fluid through thin, low-efficiency fins) has not yet been conducted. The effect of channel depth and flow length (and their interactions) on flow morphology and thermal performance have also not been studied. The current work presents a custom-designed experimental facility that provides simultaneous flow visualization and spatially resolved temperature measurements in heated manifold microchannels. Test devices, with a single channel that is representative of the repeating unit cell in a MMC heat sink, are fabricated in silicon and bonded to a solid glass cover. The flow visualizations provide insight into the flow patterns that occur in manifold microchannels during two-phase operation; the spatially resolved infrared (IR) temperature measurements allow the flow morphologies to be linked to their effect on thermal performance. Results are presented for a range

of heat fluxes for channel geometries with differing flow lengths and channel depths, at fixed channel and fin widths.

2 Experimental methods

2.1 Test device design

Manifold microchannel heat sinks distribute fluid along the length of a bank of microchannels such that the effective flow length, and thereby pressure drop, is reduced. In these heat sinks, the fluid enters the channels normal to the heated surface through an inlet manifold, impinges on the channel base, travels along the short length of the channel, and exits into an outlet manifold (Figure 1). Ideally, the manifold would provide the same amount of fluid to each channel while adding no flow resistance to the system; in practice, careful design can help reduce the manifold pressure drop while maintaining nearly uniform flow distribution. Various manifold designs have been proposed with the most common (and simple) being alternating inlet and outlet ducts running perpendicular to the heat sink channels that are connected to a single inlet header and outlet header, respectively [6]. In an effort to reduce flow maldistribution, modified versions of this design have included tapered manifold ducts [16] and hierarchical manifolds with multiple layers [18,36]. Figure 2(a) shows an exploded view of a representative manifold microchannel heat sink with a quarter-symmetry portion removed for clarity, and Figure 2(b) shows a zoomed-in view of the assembled manifold microchannel heat sink. The manifold microchannel heat sink unit cell, which is the repeating unit of the manifold microchannel heat sink, is shown Figure 2(c).
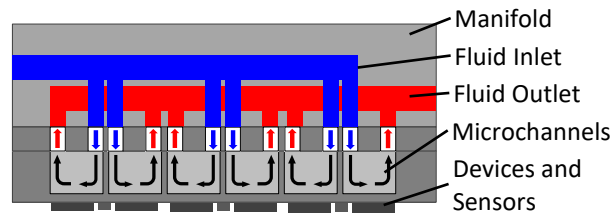
Figure 1. Schematic diagram of fluid distribution in a manifold microchannel heat sink.
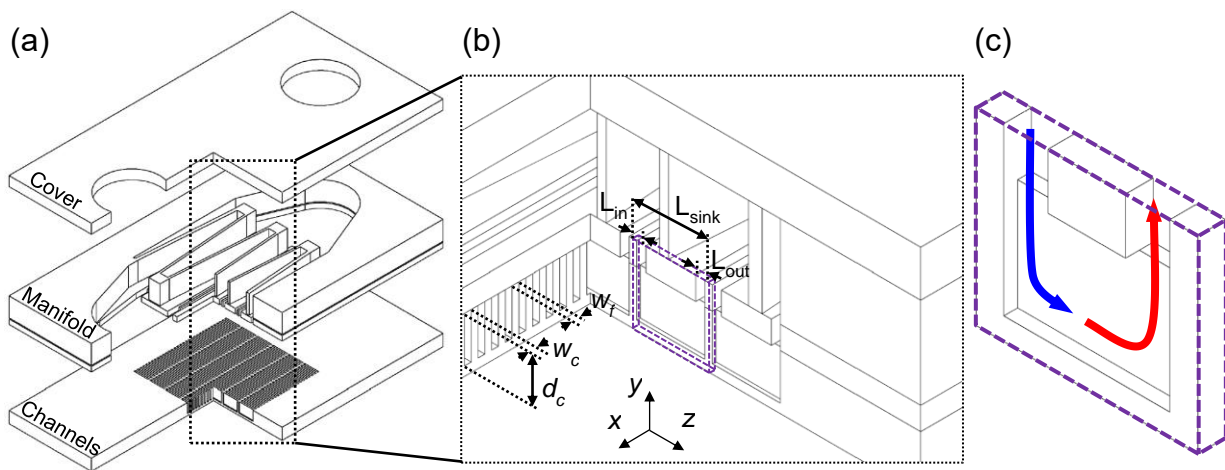*(note for editor: single-column figure)*

Figure 2. (a) Exploded view of a manifold microchannel (MMC) heat sink with a quarter-section removed, (b) an inset showing a zoomed-in view of the assembled MMC heat sink with the critical channel dimensions labeled, and (c) the MMC unit cell with the flow inlet and outlet paths shown.
(note for editor: two-column figure)

In this work, a single manifold microchannel that is representative of a repeating unit in a heat sink is fabricated in silicon with a bonded glass viewing window. Samples with different channel lengths (750 µm and 1500 µm) and depths (125 µm, 250 µm, and 1000 µm) are fabricated; channel and fin widths are both maintained at 60 µm. Subcooled fluid (HFE-7100) is delivered to the channel at a constant flow rate and a uniform heat flux is applied to the base of the channel.

9

The test device is designed to allow for simultaneous flow visualization and measurement of spatially-resolved temperatures on the backside of the channel.

Figure 3(a) shows a CAD drawing of the test device as viewed from the top side (*i.e.*, the side through which the flow can be visualized through the bonded-glass viewing window). The channel is positioned such that the channel depth is in the plane of the silicon wafer and the channel width is determined by the etch depth into the wafer; this orientation allows for optical access along the entire channel depth, which is valuable for high-aspect-ratio microchannels where large variations in wall temperature and fluid flow patterns along the channel depth may occur. Fluid enters and exits the microchannel via etched manifold features. The inset in Figure 3(b) shows a zoomed-in view of the manifold and channel features, at a slightly tilted viewing angle and with a cut-plane through the inlet manifold to reveal the base and fin thicknesses. Pressure taps are etched to the same depth as the manifold flow features and are used to measure the fluid pressure immediately before and after the channel. Holes for the inlet and outlet fluid flow paths, inlet and outlet pressure taps, and guide pins are etched through the silicon. Figure 3(c) shows the test device from the back side. The channel is heated from the bottom using an attached ceramic heater and fluid is delivered from the top using manifolds etched into the silicon. Insulation air gaps are etched through the silicon to direct heat flow from the heater toward the channel.
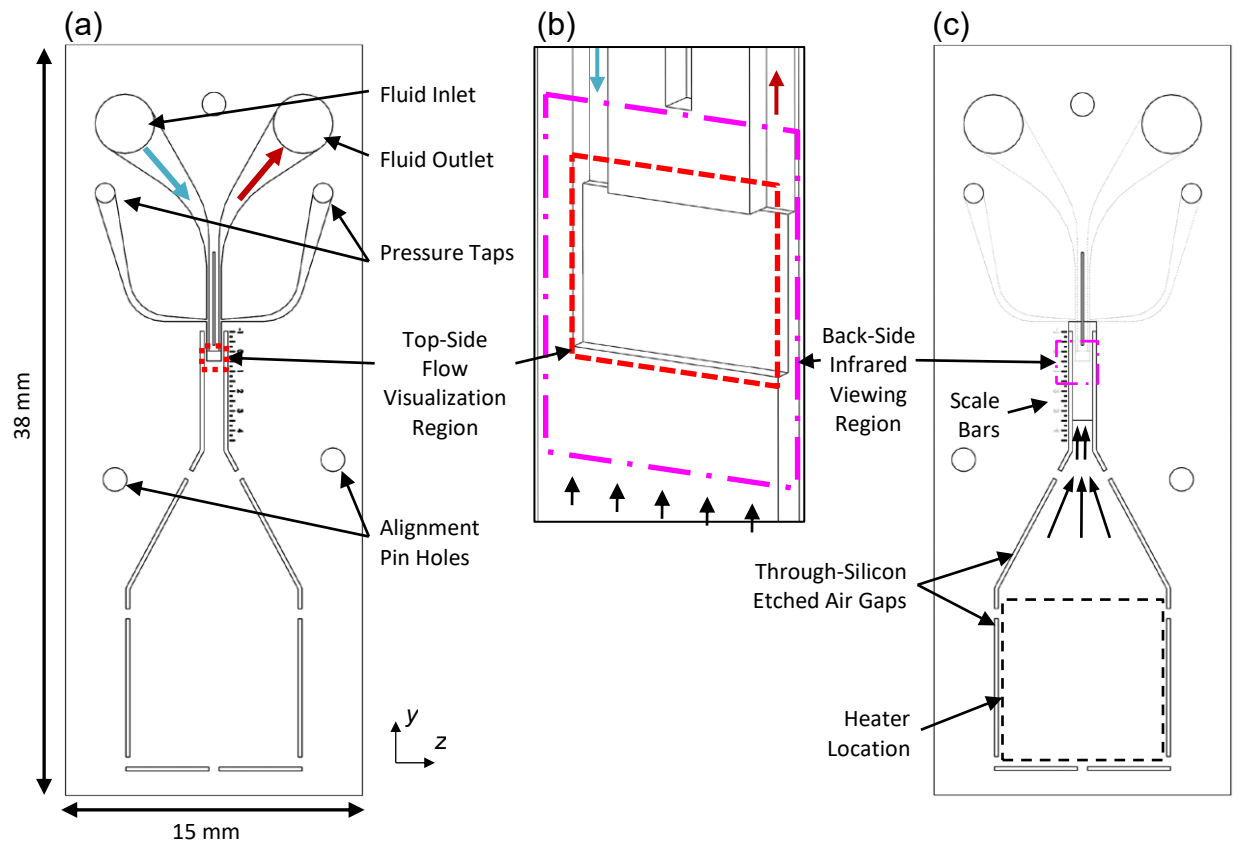
Figure 3. CAD drawings of the test device: (a) top-side view with arrows showing the fluid inlet (blue) and outlet (red) flow paths, (b) inset of the channel region viewed at an angle and with a section removed to view the channel cross-section, and (c) back-side view with arrows showing the heat flow path to the channel.
(note for editor: two-column figure)

2.2 Test device fabrication

All fabrication steps were performed in the Birck Nanotechnology Center at Purdue University. To begin the test device fabrication, a 4-inch, double-side polished silicon wafer is cleaned using a Piranha solution (3:1 H_2SO_4:H_2O_2). Photoresist (AZ 9260, 7 μm) is spun on one side of the wafer and soft baked (100 °C, 10 min). The photoresist is then exposed to the photomask containing the channel features (Suss MA6, 72 s) and developed (3:1 AZ400K:H_2O). The 4-inch

wafer is then mounted to a 6-inch carrier wafer (Crystalbond 555) and the channel features are etched (STS Advanced Silicon Etch System) to the desired channel width (Figure 4(a)). The photoresist is then cleaned (PRS-2000, 100 °C, 8 hr). This process is then repeated for the plenum features (Figure 4(b)). The wafer is then flipped over and the process is repeated, this time to remove material from the area of the wafer behind the channel to achieve the proper fin thickness of the unit cell (Figure 4(c)). The through-features are etched using the same process (Figure 4(d)); this mask includes fluid inlet and outlet holes, pressure taps, holes for alignment pins, and insulation gaps which confine the heat to the channel region. The silicon wafer and a borosilicate glass wafer are then cleaned using a Piranha solution and anodically bonded (Suss SB6e, 350 °C, 1000 V) as shown in Figure 4(e). Figure 4(f-g) show the etched features as seen from the top and back of the wafer. After bonding, the silicon side of the bonded wafer is metalized via electron-beam evaporation (PVD E-beam evaporator); a 10-nm Ti seed layer is coated with a 100-nm copper layer. The 4-inch wafer is then diced into individual test devices. A thin layer of carbon is deposited on the copper surface, resulting in an IR-opaque, high-emissivity coating. Photographs of the complete test vehicle as viewed from the channel side and fin side are shown in Figure 5(a) and (b), respectively.
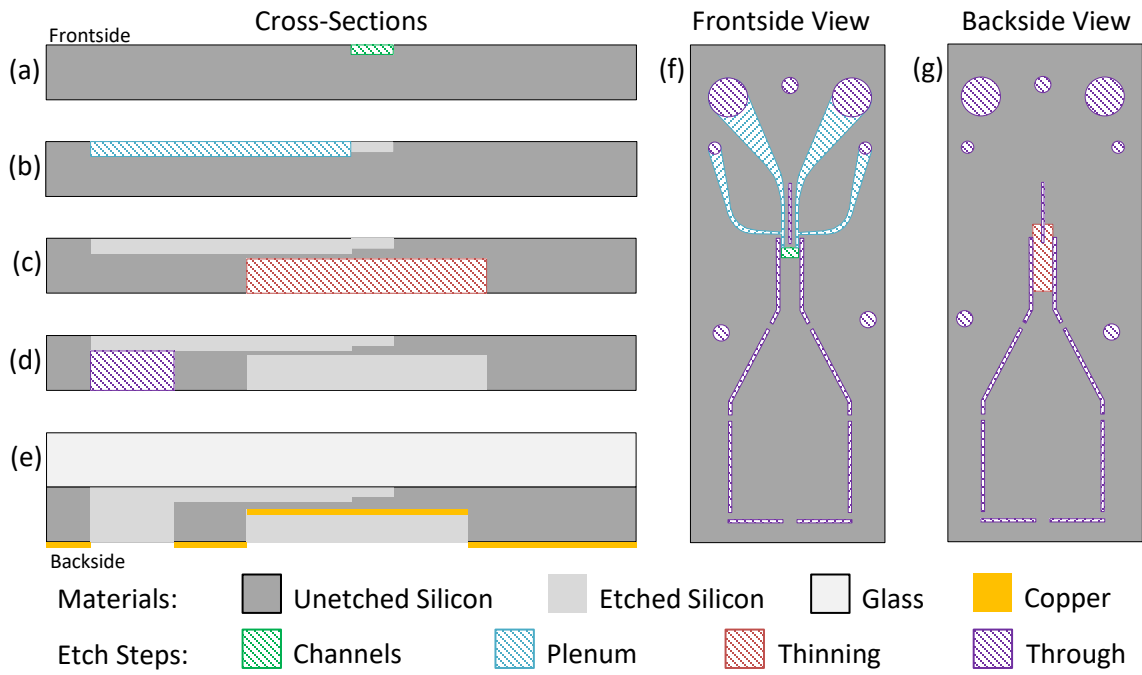
Figure 4. (a-e) Schematic diagrams showing the test device cross-sections throughout the fabrication procedure and (f) frontside- and (g) backside-view schematic diagrams after fabrication. Dimensions are not to scale.
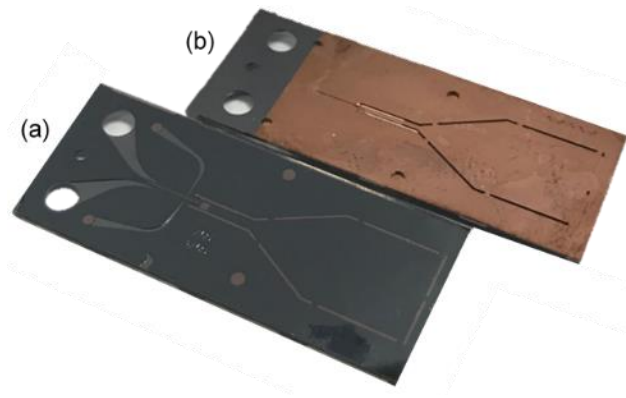*(note for editor: 1.5-column figure)*

Figure 5. Photographs of a test device viewed from the (a) front side and (b) back side.
(note for editor: single-column figure)

2.3 Assembly of the test vehicle

The test vehicle consists of the test device mounted on a PEEK test fixture, a ceramic heater (CER-1-01-00335, Watlow), and a PEEK insulation block, as well as gaskets and auxiliary fittings and hardware, as shown in Figure 6(a). The test fixture contains fluid ports, thermocouple ports, pressure taps, a cutout through which to view the sample with the IR camera, and a cutout for the ceramic heater set. A ceramic insert surrounds the heater to limit the exposure of the PEEK test fixture to high temperatures during testing; a small spring located under the heater provides the required compression force to maintain contact with the test device throughout testing. A small amount of thermal grease (AS5, Arctic Silver) is applied to the top surface of the heater during assembly to limit thermal contact resistance. A silicone gasket (thickness: 0.38 mm, hardness: 35A) is used to seal the fluid features at the surface between the test fixture and the device; the same gasket material is also placed under the ceramic insert to provide uniform deflection under the device as it is compressed. A PEEK block insulates the test device from the top and provides a method to mechanically compress and seal the test device to the fixture; the insulation block contains a viewing window to provide optical access for high-speed visualizations in the channel. Stainless steel bolts are paired with springs, washers, and bolts to compress the test device between the PEEK plates. Figure 6(b) and (c) show photographs of the assembled test vehicle from the front and back sides, respectively.

2.4 Experimental test facility

Once assembled, the test vehicle is mounted to an optical rail and all the fittings are attached (Figure 6(d)). The fluid inlet and outlet ports are connected to the flow loop, the pressure

taps are connected to the pressure transducers, and the thermocouples are placed in the inlet and outlet flow paths. A high-speed camera (Phantom v1212, Vision Research) along with a high-magnification lens (VH-Z100R, Keyence) is mounted to the optical rail facing the front side of the test vehicle. An IR camera (SC7650, FLIR) with a magnifying lens (Asio 4×, Janos) is mounted to the same optical rail facing the test vehicle from the opposite side. The IR camera is positioned such that the channel is located near the top of the window, as shown in Figure 7. The alignment of the IR camera field of view relative to the channel location is determined using the scale bars that were etched into the test device during fabrication (as shown in Figure 3); these scale bars are also used to determine the pixel size of this sensor/lens system, which was measured to be 6.41 μm/pixel. The IR camera has a resolution of 320 × 256 pixel, resulting in a viewing window that is 2.05 mm × 1.64 mm.

The flow loop is designed to deliver single-phase HFE-7100 to the test vehicle at a controllable and measurable subcooled inlet temperature, flow rate, and outlet pressure. An adjustable-volume reservoir stores the fluid and also contains immersion heaters that are used to degas the fluid prior to testing via vigorous boiling and recollection of the condensate. A gear pump (GB-P23, Micropump) delivers fluid at a constant flow rate to the test section and the flow rate is measured using a Coriolis mass flow meter (CMF010M, Micromotion). Outlet pressure is measured using a gage pressure transducer (PX302-015G, Omega) and the pressure drop across the test vehicle is measured using a differential pressure transducer (PX409-050DWU5V-EH, Omega). During testing, a fixed channel outlet pressure is maintained that is close to atmospheric pressure, corresponding to a fluid saturation temperature of 61 °C. Inlet and outlet temperatures are measured using ungrounded 500 μm-diameter thermocouples with stainless steel sheaths

15

(TJC36-CPSS-020U-6, Omega). The data are recorded using a National Instruments cDAQ-9178 chassis with the appropriate modules and are monitored using a custom LabVIEW interface. Steady-state temperature, pressure, and flow rate data are collected at 3,000 Hz and averaged over a 20 s period. Flow visualizations are recorded at 56,000 – 76,000 frames per second, depending on the resolution of the images being captured; the IR images are recorded at 10 frames per second and are averaged over 20 s to provide a single time-averaged, spatially-resolved temperature map for each test condition.
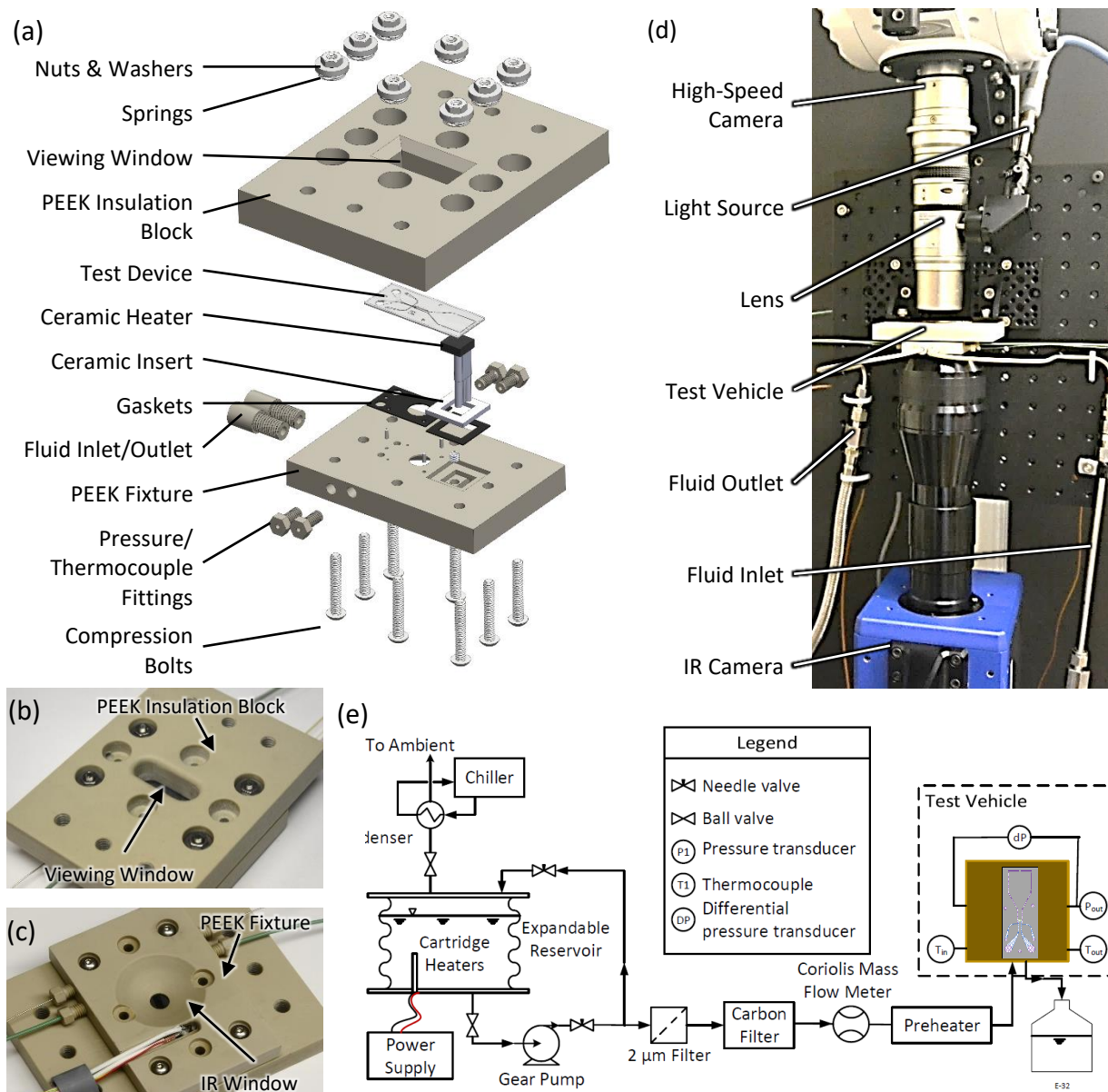
Figure 6. (a) Exploded view of the test vehicle assembly, and photographs of the test vehicle from the (b) front side, which contains a viewing window for high-speed visualizations and (c) back side, showing the pressure taps, thermocouples, heater leads, and IR viewing window. (d) Photograph of the test vehicle assembled in the flow loop with the IR camera and high-speed camera mounted, and (e) a schematic diagram of the experimental flow loop.
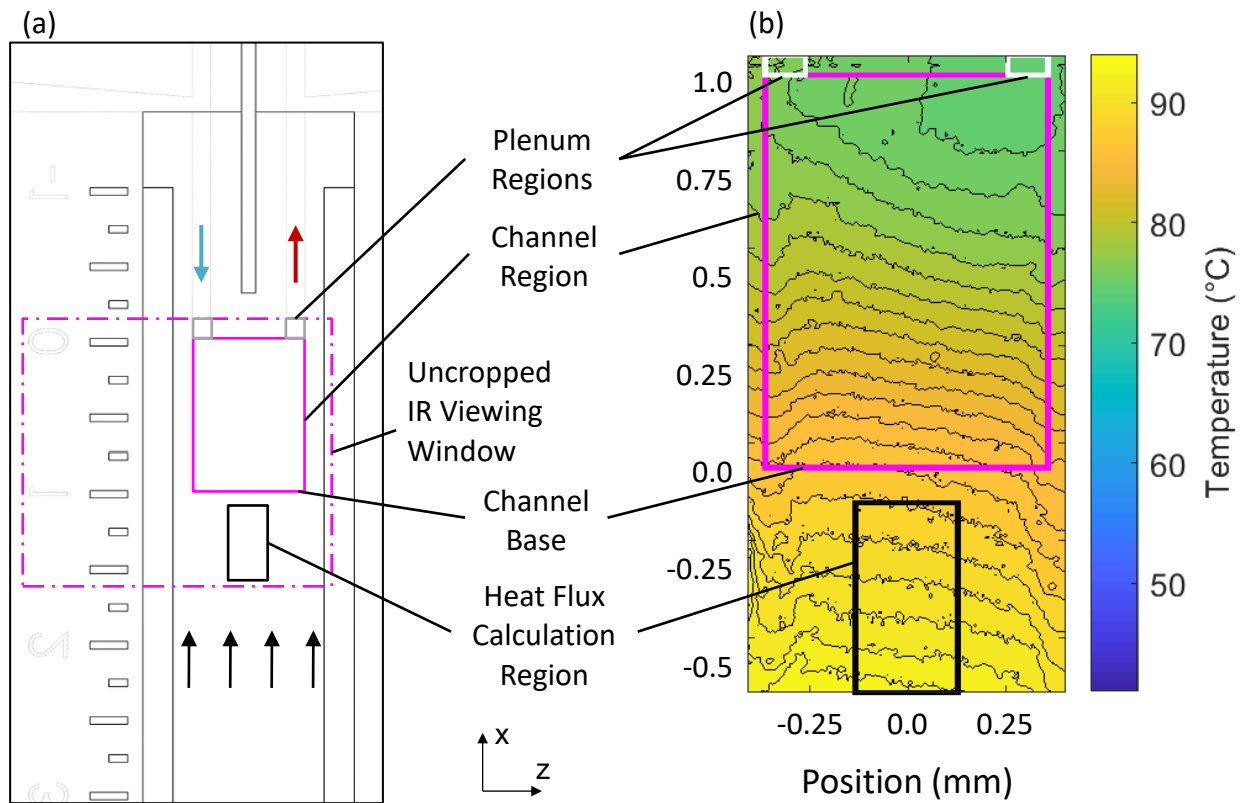*(note for editor: two-column figure)*

Figure 7. (a) CAD model of a test device (Sample 3, 750 × 1000 μm) viewed from the back side showing the position of the uncropped IR viewing window and (b) a sample temperature map showing the region used to calculate heat flux into the channel and the channel region.
(note for editor: 1.5-column figure)

2.5 Infrared camera calibration

To calibrate the IR camera, a dummy sample device is mounted to a copper sheet using thermal grease; this dummy sample was fabricated on the same wafer as the test devices and therefore went through the same processing and post-treatment steps. A thermocouple (TJC36-CPSS-020U-6, Omega) is placed on the sample surface with a small bead of thermal paste on the tip. A resistive heater is attached to the opposite side of the copper sheet. This fixture is then placed on the optical rail above the infrared camera and brought into focus. The integration time,

18

measurement frequency, and measurement time for the camera are set (175 µs, 10 Hz, 20 s). The power to the heater is increased in increments that resulted in 10 temperatures spanning the range of temperatures experienced during testing (35 °C – 120 °C). The intensity is measured for each pixel across the IR field of view for each steady-state point, which is referenced to the uniform sample surface temperature as measured by the thermocouple. The calibration determines the nonuniformity across the infrared image and a fourth-order polynomial is fitted for each pixel. Because the calibration sample and the test device have the same surface properties, the emissivities are identical.

2.6 Data reduction and uncertainty

The heat flux into the channel base is directly measured using the IR temperature data, which avoids the need to estimate the heat loss from the resistive heater. This heat flux is calculated based on the temperatures spanning from 100 µm below the channel bottom to the lower edge of the IR viewing region (Figure 7(b)); the region nearest the channel is excluded due to the nonuniformity caused by three-dimensional conduction effects resulting from the channel geometry and nonuniform heat transfer coefficients in the channel. To limit the contribution of edge effects, only the central region is used in the heat flux calculation. The temperatures in the area of interest are averaged across the z-direction, resulting in an array of z-averaged temperatures along the x-direction. Figure 8 shows representative z-averaged temperatures as a function of x position in the heat flux region; the dashed line shows the first-order linear regression that is fit to these data with the slope being the temperature gradient. Once the temperature gradient is calculated, base heat flux can be calculated assuming one-dimensional heat conduction:

$q''_{base} = -k_{Si} \dfrac{dT(x)}{dx}$. The channel base temperature is calculated by averaging the temperatures at

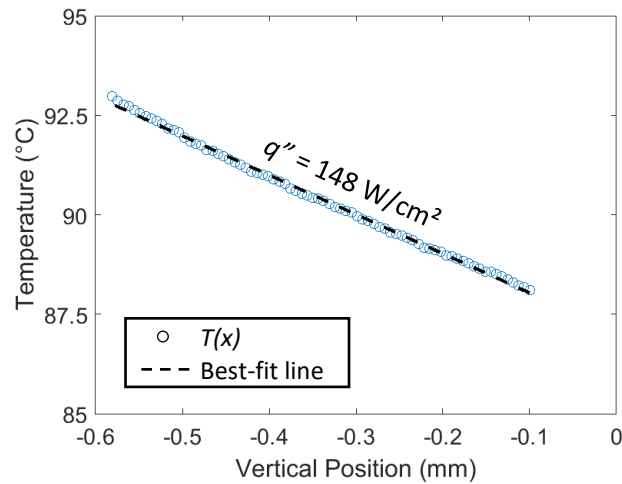the bottom of the channel region in the *z*-direction.

Figure 8. A representative set of *z*-averaged temperature measurements as a function of vertical position for Sample 3 at one representative heat flux, along with the best-fit line. The vertical position is shown relative to the channel base at zero, as defined in Figure 7.
(note for editor: single-column figure)

The measurement uncertainties of each instrument in the experimental test facility, per the manufacturers' specifications, are listed in Table 1. The uncertainty in the wall temperature is estimated based on the uncertainty in the calibration procedure as well as the uncertainty in the reference thermocouple. The uncertainty in the heat flux calculation is based on the goodness of the linear fit and uncertainties in the wall temperature measurements, positions, and pixel size.

Table 1. Uncertainty in measured and calculated data

Measurement	Instrument	Manufacturer	Uncertainty
Wall temperature	IR camera	FLIR	± 1.5 °C
Location	-	-	10 μm
Heat flux	-	-	± 5 W/cm²
Fluid inlet temperature	T-type thermocouple	Omega	± 0.5 °C
Fluid outlet temperature	T-type thermocouple	Omega	± 0.5 °C
Pressure drop	Differential pressure transducer	Omega	± 0.17 kPa
Mass flow rate	Coriolis mass flow meter	Micromotion	± 5.0 %

2.7 Test matrix

The critical dimensions of the three devices tested are shown in Table 2. These channel geometries were chosen to provide a range of aspect ratios ($AR = d_c/w_c$) and nondimensional lengths ($L_{nd} = L_c/d_c$). Increasing the aspect ratio will reveal its effect on the flow morphology and wall temperature drop along the channel depth. A change in nondimensional length allows evaluation of its effect on the flow distribution along the channel depth. Sample 1 consists of a microchannel that closely resembles a traditional microchannel, with a large nondimensional length and relatively low aspect ratio. Sample 3, on the other hand, is a high-aspect-ratio microchannel (AR = 16.7) with an extremely small nondimensional length less than unity (*i.e.*, the channel is deeper than it is long). Sample 2 provides an intermediate case. The samples are tested at flow rates that result in a fluid velocity of ~1.05 m/s at the inlet to the channel in all cases (Sample 1: $G = 4470$ kg/m²s, Sample 2: $G = 1290$ kg/m²s, Sample 3: $G = 320$ kg/m²s).

Table 2. Summary of microchannel dimensions.

Sample	Channel Length L_c (μm)	Inlet Plenum Length L_{in} (μm)	Outlet Plenum Length L_{out} (μm)	Channel Depth d_c (μm)	Channel Width w_c (μm)	Aspect Ratio $AR = d_c/w_c$ (-)	Non-dimensional Length $L_{nd} = L_c/d_c$ (-)
1	1500	400	400	125	60	2.1	12
2	750	200	200	250	60	4.2	3
3	750	200	200	1000	60	16.7	0.75

3. Results and discussion

We first describe the spatially and temporally averaged steady-state data; trends in base superheat temperature and pressure drop as a function of heat flux and channel geometry are presented (Section 3.1). Flow visualization images and spatially resolved wall temperature are then presented for each of the channel geometries to explain the mechanisms leading to the thermal-hydraulic trends (Section 3.2). The critical differences in two-phase flow morphology between standard microchannels and high-aspect-ratio manifold microchannels are then discussed (Section 3.3).

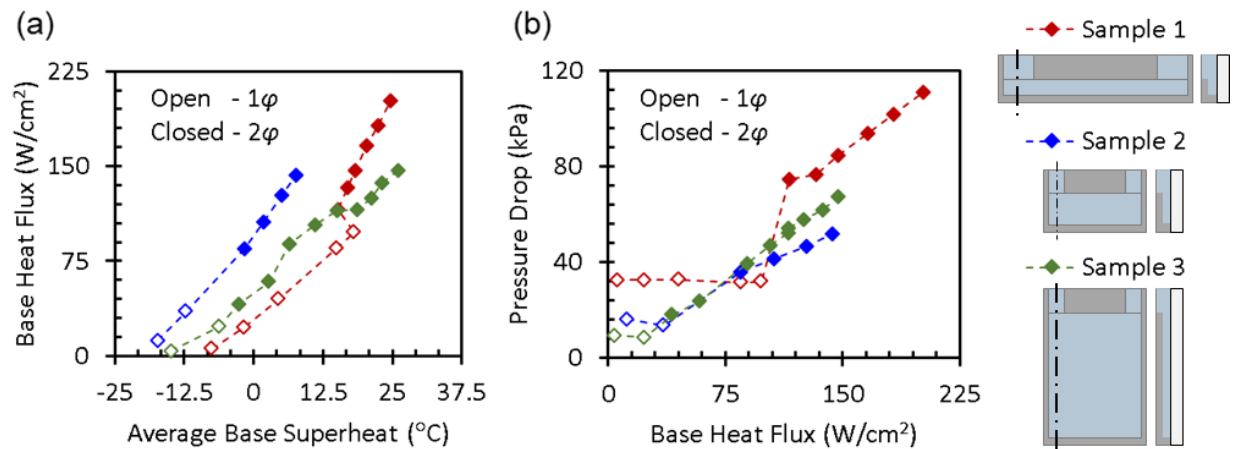## 3.1 Time-averaged steady-state experimental results

Figure 9(a) shows channel base superheat temperatures for the range of heat fluxes tested for each sample. The open symbols signify single-phase operation and the closed symbols represent two-phase operation. For all samples, testing was terminated to avoid exceeding the heater temperature limit, not because critical heat flux was reached in the channel.

Sample 1 remains in single-phase operation up to 100 W/cm²; in this single-phase region, the temperature rise with increasing heat flux is linear, as is characteristic of single-phase flow. Upon boiling insipience at 100 W/cm², the base superheat decreases. During two-phase operation, the slope of the boiling curve increases compared to single-phase operation because of the increased heat transfer coefficient during flow boiling. Boiling is initiated in Samples 2 and 3 at approximately 40 W/cm², upon which both samples show a slight increase in slope. During two-phase operation, Sample 3 exhibits a much more irregular temperature response to applied heat flux, which is not seen in most traditional microchannel systems; between 75 and 116 W/cm², the temperature rises linearly at which point the superheat rises 3 °C with a slight increase in heat flux; above 116 W/cm², the temperature rise is again linear.
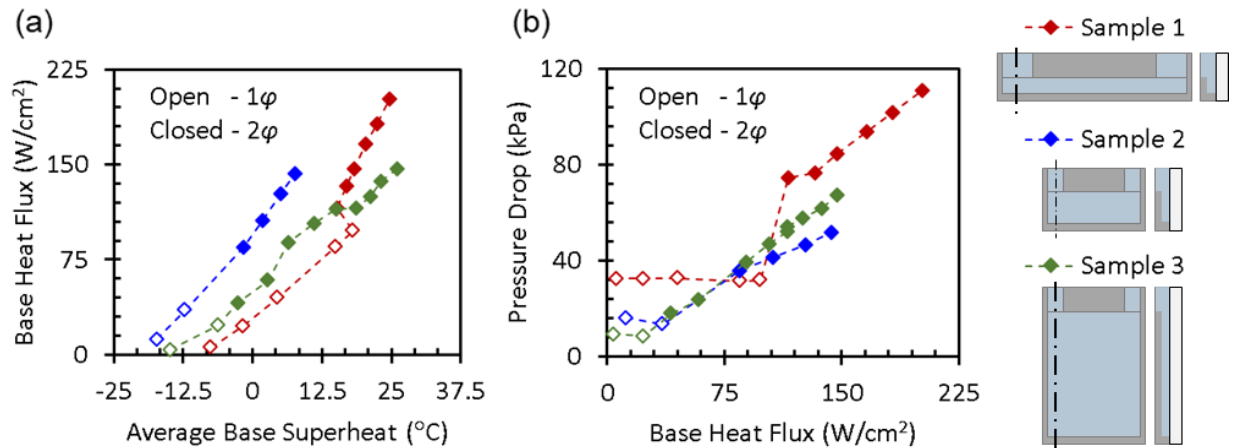
Figure 9(b) shows the pressure drop as a function of heat flux for the three samples. During single-phase operation, the pressure drop remains relatively constant with heat flux for each sample. Upon boiling incipience, the pressure drop increases sharply due to the effective acceleration in the fluid velocity associated with vapor generation in the channel. The pressure drop increases linearly with increasing heat flux in the two-phase regime due to the increase in vapor quality leading to larger velocities.
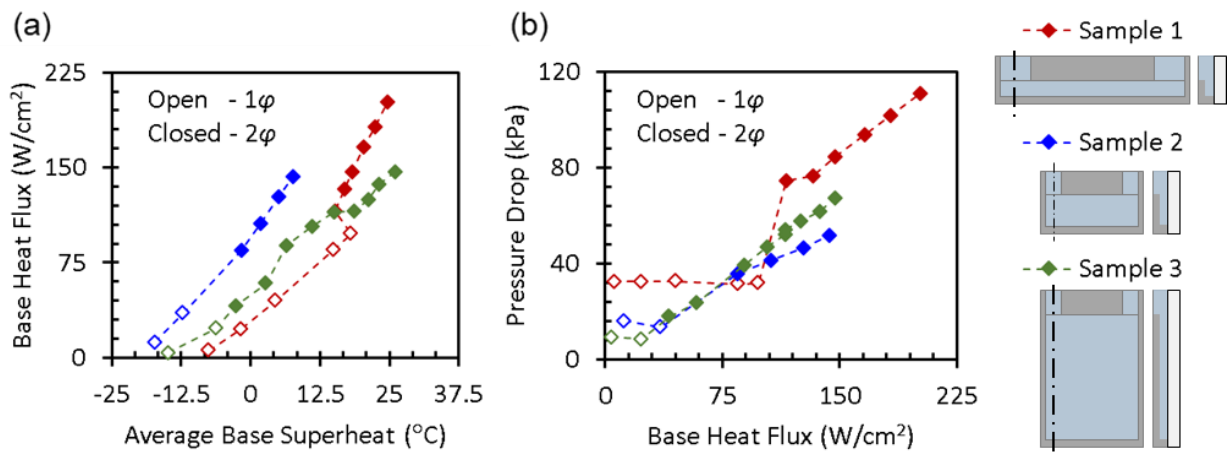

24

Figure 9. (a) Base heat flux as a function of average base superheat temperature and (b) pressure drop as a function of base heat flux for each channel geometry. The sketches embedded in the legend for each sample show a view of the channel from the front (left) and a cross sectional view when cut through the inlet plenum (right).
(note for editor: two-column figure)

3.2 Flow morphology and spatially resolved wall temperatures

3.2.1 Low-aspect-ratio microchannel (Sample 1)

Figure 10(a) shows the measured wall temperature distributions for Sample 1, normalized against the maximum wall temperature measured at that operating point, for all steady-state operating points shown in
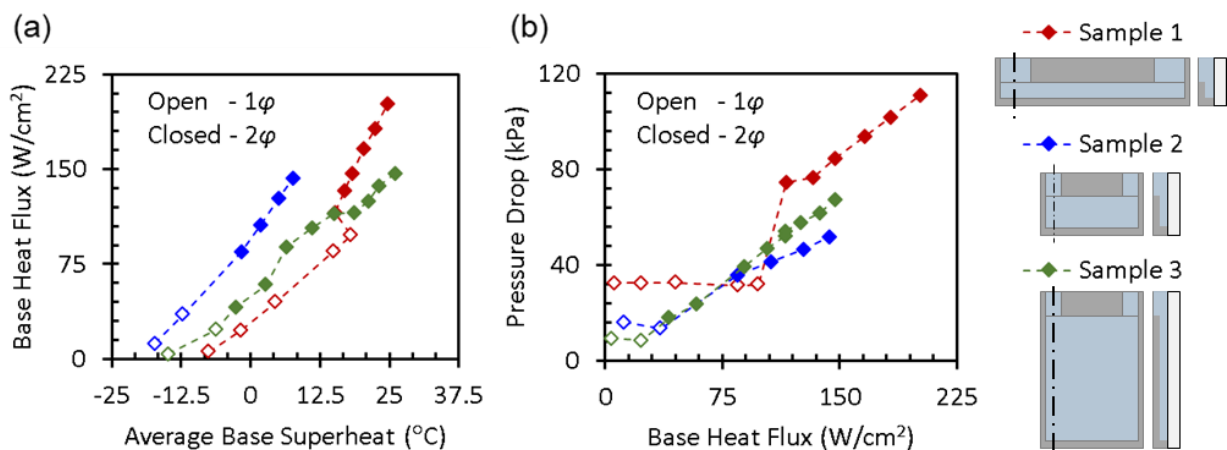

Figure 9; flow visualizations are shown for all operating points where boiling occurs (Figure 10(b)). During single-phase operation, for heat fluxes from 6 – 98 W/cm², subcooled fluid enters the channel and is heated along its length, as shown in the temperature maps in Figure 10(a). At the lowest heat flux after incipience (116 W/cm²), vapor first nucleates at the top surface of the channel where the fluid flows past a sharp corner at the inlet, followed by activation of additional nucleation sites at the bottom corner near the exit plenum and at the top of the fin at the exit. Vapor

25

bubbles nucleate at these sites, grow, depart, and become entrained in the bulk flow. At the outlet plenum, the flow becomes well-mixed due to the bend in the flow path. As heat flux is increased (116 – 202 W/cm²), the number of nucleation sites increases and the sites move toward the inlet plenum. For all heat fluxes, the flow is stable and has the same behavior over time (refer to Appendix A for high-speed videos of the flow morphology).

While the normalized wall temperature profiles are similar for all heat fluxes during single-phase operation, the single-phase and two-phase wall temperature profiles differ drastically from each other. During single-phase operation (<98 W/cm²), the region immediately under the fluid inlet is consistently the coolest region due to the fluid arriving subcooled as well as impingement and developing flow effects; conversely, this same region becomes the hottest during two-phase operation. At heat fluxes of 116 and 133 W/cm², boiling is suppressed in the region under the inlet, which could cause a relatively higher temperature compared to the downstream regions with boiling; above 133 W/cm², a relatively stable vapor bubble embryo forms in this region, which could also lead to the local relative increase in temperature. During saturated flow boiling, the fluid will cool down along the length of a channel due to the decrease in saturation temperature with decreasing pressure; each two-phase temperature profile shows a decrease in temperature along the length of the channel and also a sharp drop near the expansion to the outlet plenum. Note that the temperature drop along the depth of the channel is less than 2 °C for all heat fluxes, for this shallow channel depth.
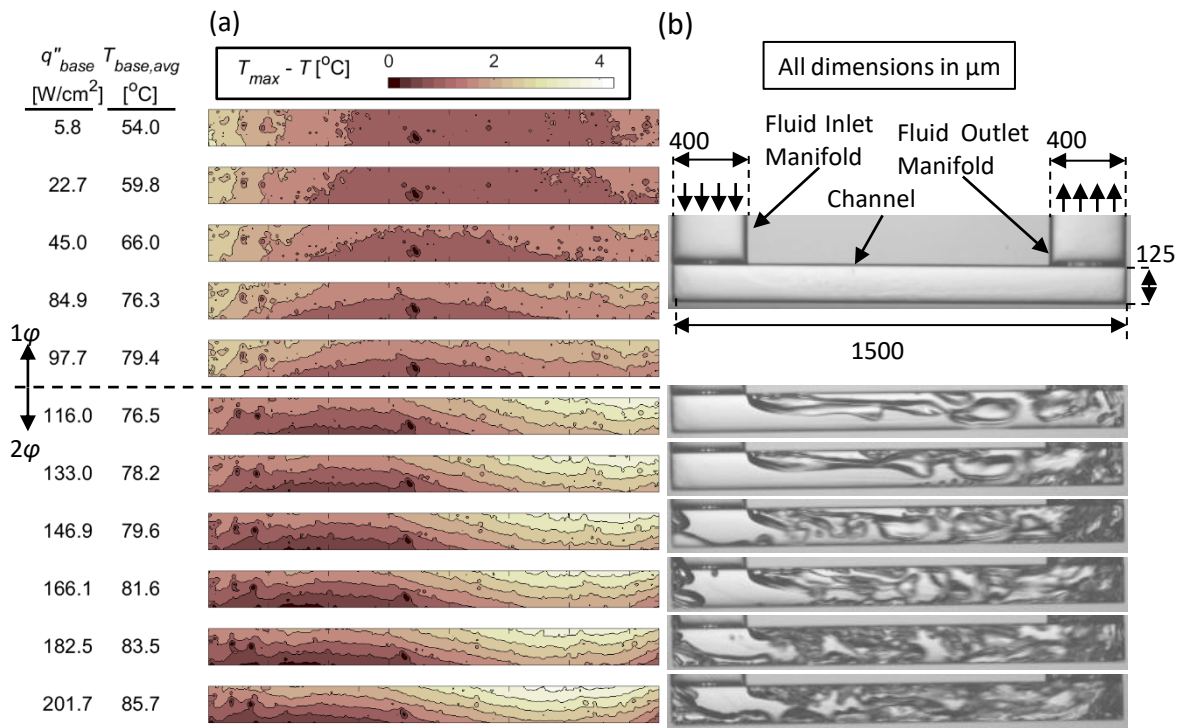
Figure 10. (a) Wall temperature maps for Sample 1 (1500 μm × 125 μm) over the range of heat flux inputs shown in
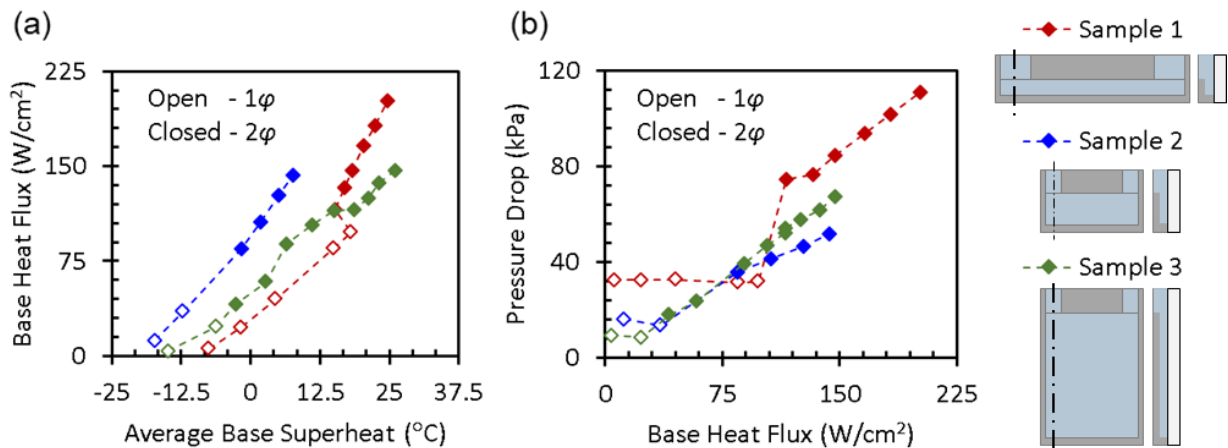

Figure 9. The relative temperature range remains constant while the absolute temperature scales change for each plot. (b) Flow visualization images are shown during two-phase operation.
(note for editor: 1.5-column figure)

3.2.2 Medium-aspect-ratio microchannel (Sample 2)

Figure 11 shows the time-averaged wall temperature maps (Figure 11(a)) and images of the two-phase flow (Figure 11(b)) for Sample 2. The wall temperatures are normalized to the maximum temperature measured at each heat flux. The wall temperatures are uniform during single-phase operation (12 - 35 W/cm²), with all local wall temperatures within 2 °C (note that there is a low-temperature artifact near the outlet end of the channel in all of the data for this case, due to a defect in the high-emissivity carbon coating at this location). As was the case for Sample 1, the wall temperature profile changes significantly upon incipience, after which the region near the outlet plenum has the highest relative wall temperature. This trend of decreasing wall temperature along the flow length is present throughout two-phase operation (85 – 143 W/cm²). The maximum temperature difference is approximately 6 °C at the highest heat flux.

From the visualizations (Figure 11(b); refer to Appendix A for high-speed videos), at the first steady-state heat flux after incipience (85 W/cm²), vapor nucleates at the sidewall beneath the inlet plenum and is dragged into the bulk flow. A relatively stagnant vapor bubble is pinned to the region under the channel top wall; vapor is pinched off from the trailing edge of this bubble where the top wall and outlet plenum meet and entrained into the exiting flow. As the heat flux is increased (106 - 127 W/cm²), discrete bubbles are visible in the bottom of the channel throughout most of the flow length, with mixing occurring near the end of the channel under the outlet plenum. At the highest heat flux of 143 W/cm², the stagnant vapor bubble attached to the channel top wall is disrupted by the large amounts of vapor generated, leading to slightly lower relative temperatures in this region. Also, at the highest heat flux, the flow begins to periodically fluctuate due to temporary vapor clogging at the outlet manifold. Local dryout is not observed anywhere in

the channel (aside from the small region underneath the channel top wall, where the stagnant

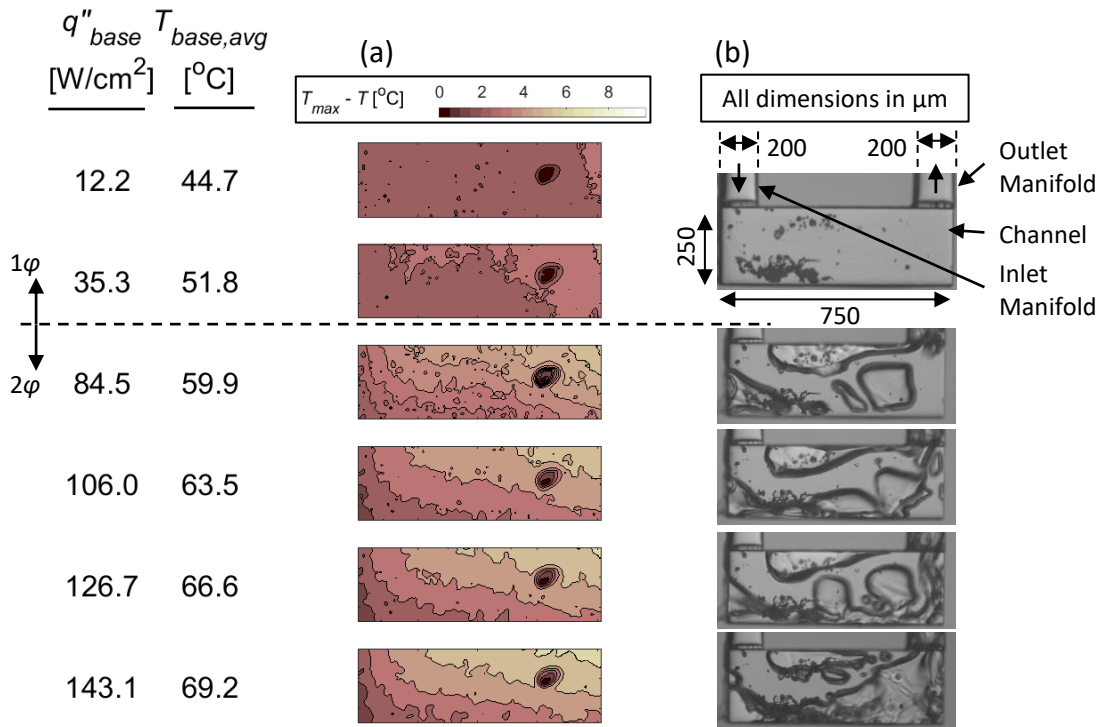bubble occupies the entire channel width for all two-phase operating points).

Figure 11. (a) Wall temperature maps for Sample 2 (750 μm × 250 μm) over the range of heat flux inputs shown in
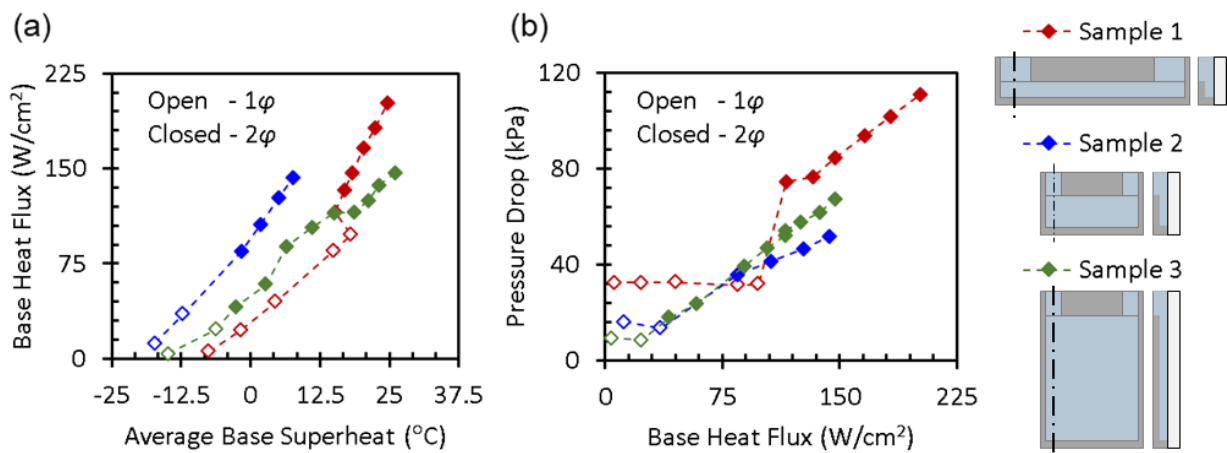
Figure 9. The relative temperature range remains constant while the absolute temperature scales change for each plot. (b) Flow visualization images are shown during two-phase operation.
(note for editor: 1.5-column figure)

3.2.3 High-aspect-ratio microchannel (Sample 3)

While the two-phase flow morphologies for Samples 1 and 2 were largely invariant in time, the flow morphology for Sample 3 exhibits extreme, time-periodic variations. Figure 12 shows a sequence of images for three selected heat fluxes along with the time-averaged wall temperatures at these heat fluxes. In Figure 12(a), at 89 W/cm², the channel starts (0.00 ms) with the bottom portion largely covered in vapor, with most of the fluid bypassing the bottom half of the channel; nucleation primarily occurs at the sidewall near the outlet and below the manifold near the inlet. The large amount of vapor being generated bridges the entire channel depth, temporarily restricting the flow (0.27 ms). This restriction causes the liquid arriving from the inlet to move toward the channel bottom, impinge on the bottom of the channel (0.54 ms), and spread along the channel base (1.07 ms). The vapor blanket is then re-formed (2.75 ms) and the cycle repeats. The resulting temperature map shows a steep temperature gradient along the channel depth from the base to the fin tips; there is little gradient in temperature along the flow direction. The trends for the next higher heat flux of 115 W/cm² are largely the same, with a vapor blanket present along the bottom of the channel and a periodic rewetting of the entire channel base (Figure 12(b)). At the highest heat flux tested for this channel geometry (148 W/cm²), the liquid is not able to rewet the entire channel base, as shown in Figure 12(c). Unlike at the lower heat fluxes, a large region near the bottom corner under the inlet is continuously coated in vapor and the channel base is only rewetted in a small region under the outlet. This leads to a slight temperature gradient along the channel

length at the highest heat flux, with the hottest region being near the channel base close to the inlet (in addition to the extreme temperature gradient along the channel depth, which persists).
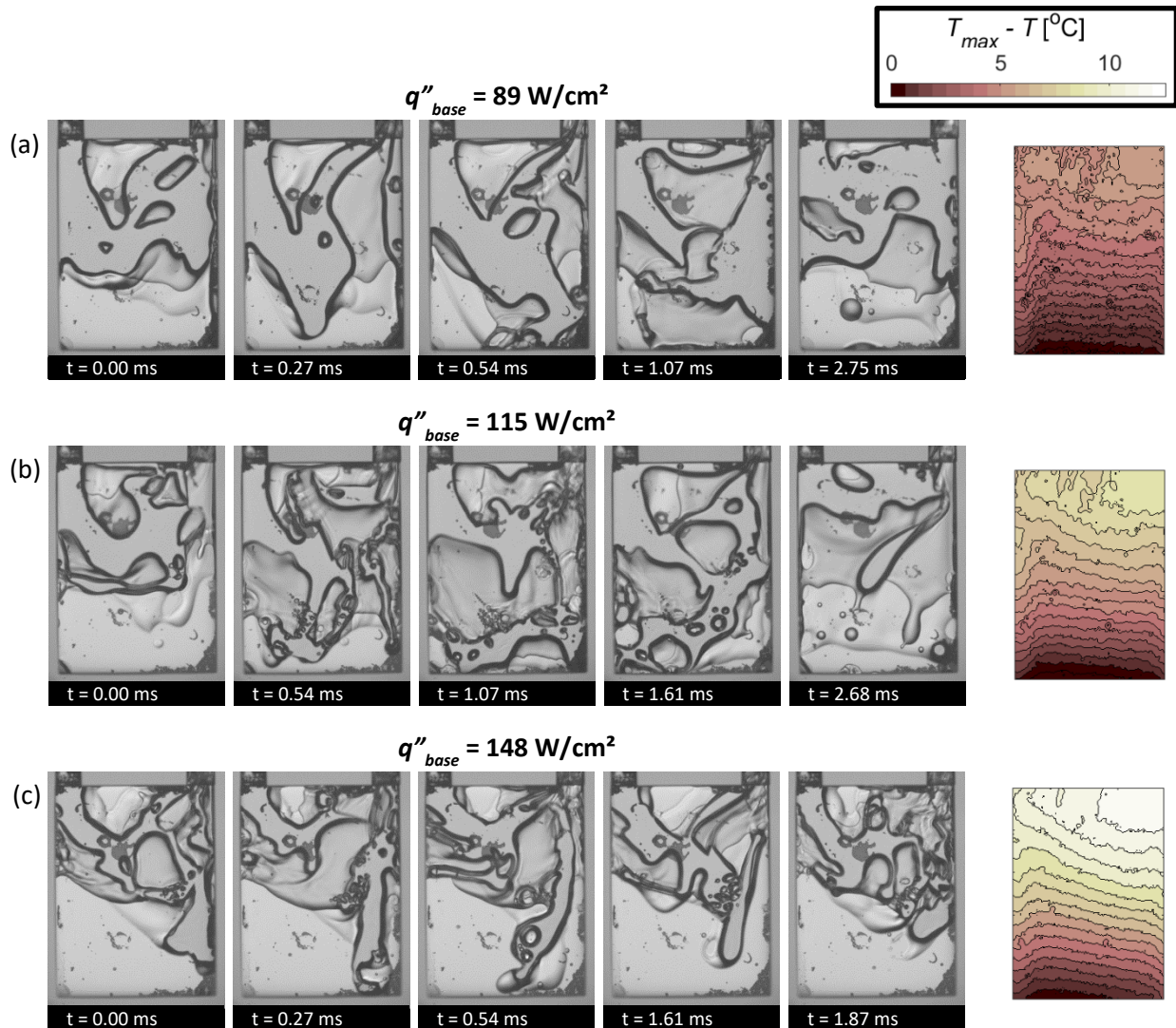

Figure 12. High-speed images showing the two-phase flow inside the channel of Sample 3 (750 μm × 1000 μm) along with the corresponding time-averaged wall temperature map for each heat flux. Data are shown for base heat fluxes of (a) 89 W/cm², (b) 115 W/cm², and (c) 148 W/cm². High-speed videos are available; refer to Appendix A.
(note for editor: two-column figure)

3.3 Discussion

In traditional heat sinks, increasing channel depth provides a straightforward means of increasing surface area in order to dissipate higher heat fluxes. For manifold microchannel heat sinks, where the fluid arrives at the top of the channel, the two-phase flow morphology plays a large role in determining heat transfer performance and the optimal channel depth. This is clearly exhibited in the data for Sample 2, which has a wetted area that is four times less than in Sample 3, but nevertheless consistently provides lower wall temperatures at the same flow rate and similar pressure drops during two-phase operation (
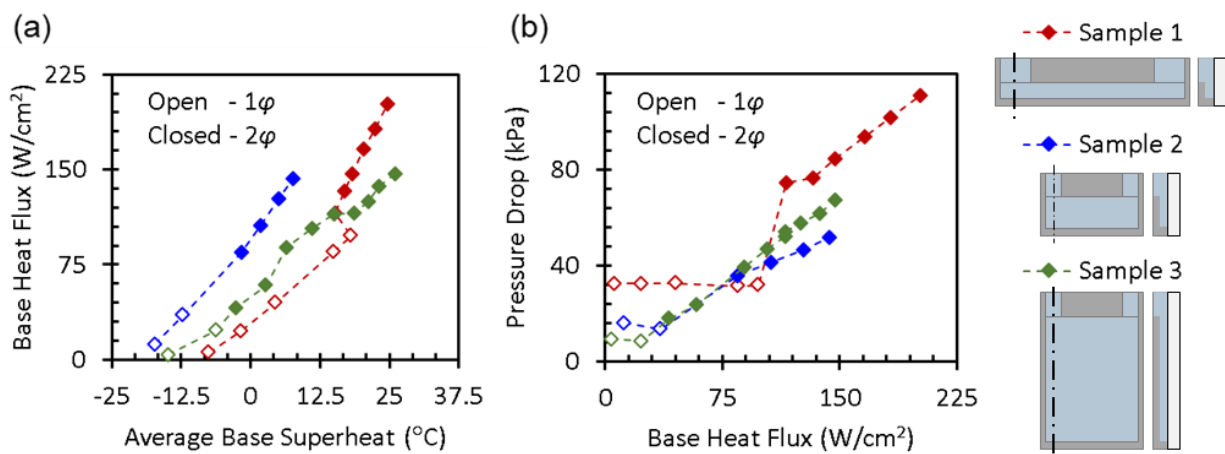

Figure 9), which would not be expected in traditional microchannels. We attribute this to

the lack of local dryout at the channel base for Sample 2 (Figure 11), compared to the consistent

vapor blanketing that occurs at the bottom of the channel for Sample 3 (Figure 12). Because the

local heat transfer coefficient in this vapor-blanketed region would be extremely poor, this wall

area does not effectively contribute to the overall heat removal. Furthermore, because the vapor

blanket is located at the bottom of the channel where the heat is applied, this blanketing has the

added consequence of forcing all heat to bypass through the thin fin to be dissipated higher up in

the channel, causing a large temperature gradient along the fin height (Sample 3 has a temperature

drop of ~12 °C along the fin height versus ~3 °C for Sample 2 at a similar heat flux). This work

highlights the importance of comprehensive mapping of the flow morphologies in manifold microchannel heat sinks to enable design for two-phase operation.

4 Conclusions

Simultaneous high-speed visualizations of the flow morphology and infrared channel wall temperature maps are presented for two-phase flow in a manifold microchannel. Test devices with different flow lengths and channel depths are experimentally investigated using HFE-7100 as the working fluid. During single-phase operation, the wall region near the inlet manifold has the coldest temperatures and the wall becomes hotter along the fluid flow length. For shallow, long channels, the two-phase flow morphology follows conventional regimes for straight channels. However, for deeper, shorter-length channels, vapor becomes intermittently trapped at the bottom portion of the channel, thereby limiting the local heat transfer and increasing the wall temperature near the channel base. In extreme channel geometries, the vapor blanket in some regions is never able to rewet the channel base, leading to high local wall temperatures in these regions. The consequence of this flow behavior is demonstrated when comparing the two samples with equal flow lengths (750 μm) and channel depths of 250 μm and 1000 μm. While the deeper of the two channels has ~4 times the surface area, the base temperatures for this deeper channel remain hotter for a given base heat flux, due to the vapor blanketing at the bottom of the channel. For manifold microchannels, the two-phase flow morphology plays a critical role in determining heat transfer performance and must be carefully considered in heat sink design.

Acknowledgements

Appendix A

The supplementary high-speed videos associated with the article can be found online.

References

[1] A. Bar-Cohen, J.J. Maurer, J.G. Felbinger, DARPA's intra/interchip enhanced cooling (ICECool) program, Proceedings of the Compound Semiconductor Manufacturing Technology Conference (CS MANTECH), (2013) 171-174.

[2] K.P. Bloschock, A. Bar-Cohen, Advanced thermal management technologies for defense electronics, Proceedings of SPIE 8405, Defense Transformation and Net-Centric Systems, (2012) 84050I-84050I–12.

[3] J.H. Ryu, D.H. Choi, S.J. Kim, Three-dimensional numerical optimization of a manifold microchannel heat sink, Int. J. Heat Mass Transf. 46 (2003) 1553–1562.

[4] R.S. Andhare, A. Shooshtari, S.V. Dessiatoun, M.M. Ohadi, Heat transfer and pressure drop characteristics of a flat plate manifold microchannel heat exchanger in counter flow configuration, Appl. Therm. Eng. 96 (2016) 178–189.

[5] T. Baummer, E. Cetegen, M. Ohadi, S. Dessiatoun, Force-fed evaporation and condensation utilizing advanced micro-structured surfaces and micro-channels, Microelectron. J. 39 (2008) 975–980.

[6] T. Brunschwiler, B. Michel, D. Poulikakos, Experimental investigation of an ultrathin manifold microchannel heat sink for liquid-cooled chips, J. Heat Transf. 132 (2010) 081402.

[7] D.B. Tuckerman, R.F.W. Pease, High-performance heat sinking for VLSI, IEEE Electron Device Lett. 2 (1981) 126–129.

[8] G.L. Morini, Single-phase convective heat transfer in microchannels: a review of experimental results, Int. J. Therm. Sci. 43 (2004) 631–651.

[9] D. Copeland, M. Behnia, W. Nakayama, Manifold microchannel heat sinks: isothermal analysis, IEEE Trans. On. Compon. Packag. Manuf. Technol. 20 (1997) 96–102.

[10] G.M. Harpole, J.E. Eninger, Micro-channel heat exchanger optimization, in: IEEE Semicond. Therm. Meas. Manag. Symp. (1991) 59–63.

[11] W. Escher, B. Michel, D. Poulikakos, A novel high performance, ultra thin heat sink for electronics, Int. J. Heat Fluid Flow. 31 (2010) 586–598.

[12] L. Boteler, N. Jankowski, P. McCluskey, B. Morgan, Numerical investigation and sensitivity analysis of manifold microchannel coolers, Int. J. Heat Mass Transf. 55 (2012) 7698–7708.

[13] C.S. Sharma, M.K. Tiwari, B. Michel, D. Poulikakos, Thermofluidics and energetics of a manifold microchannel heat sink for electronics with recovered hot water as working fluid, Int. J. Heat Mass Transf. 58 (2013) 135–51.

[14] S. Sarangi, K.K. Bodla, S.V. Garimella, J.Y. Murthy, Manifold microchannel heat sink design using optimization under uncertainty, Int. J. Heat Mass Transf. 69 (2014) 92–105.

[15] M.A. Arie, A.H. Shooshtari, S.V. Dessiatoun, E. Al-Hajri, M.M. Ohadi, Numerical modeling and thermal optimization of a single-phase flow manifold-microchannel plate heat exchanger, Int. J. Heat Mass Transf. 81 (2015) 478–489.

[16] W. Tang, L. Sun, H. Liu, G. Xie, Z. Mo, J. Tang, Improvement of flow distribution and heat transfer performance of a self-similarity heat sink with a modification to its structure, Appl. Therm. Eng. 121 (2017) 163–171.

[17] Y. Zhang, S. Wang, P. Ding, Effects of channel shape on the cooling performance of hybrid micro-channel and slot-jet module, Int. J. Heat Mass Transf. 113 (2017) 295–309.

[18] K.P. Drummond, D. Back, M.D. Sinanis, D.B. Janes, D. Peroulis, J.A. Weibel, S.V. Garimella, A hierarchical manifold microchannel heat sink array for high-heat-flux two-phase cooling of electronics, Int. J. Heat Mass Transf. 117 (2018) 319–330.

[19] K.P. Drummond, D. Back, M.D. Sinanis, D.B. Janes, D. Peroulis, J.A. Weibel, S.V. Garimella, Characterization of hierarchical manifold microchannel heat sink arrays under simultaneous background and hotspot heating conditions, Int. J. Heat Mass Transf. 126, Part A (2018) 1289–1301.

[20] S.V. Garimella, T. Harirchian, Microchannel Heat Sinks for Electronics Cooling, in: Encycl. Therm. Packag., World Scientific, 2014: p. 248.

[21] R.S. Patel, J.A. Weibel, S.V. Garimella, Mechanistic modeling of the liquid film shape and heat transfer coefficient in annular-regime microchannel flow boiling, Int. J. Heat Mass Transf. 114 (2017) 841–851.

[22] J. Moreno Quibén, J.R. Thome, Flow pattern based two-phase frictional pressure drop model for horizontal tubes. Part I: Diabatic and adiabatic experimental study, Int. J. Heat Fluid Flow. 28 (2007) 1049–1059.

[23] T. Harirchian, S.V. Garimella, Effects of channel dimension, heat flux, and mass flux on flow boiling regimes in microchannels, Int. J. Multiph. Flow. 35 (2009) 349–362.

[24] T. Harirchian, S. Garimella, Flow regime-based modeling of heat transfer and pressure drop in microchannel flow boiling, Int. J. Heat Mass Transf. 55 (2012) 1246–1260.

[25] S. Szczukiewicz, N. Borhani, J.R. Thome, Two-phase heat transfer and high-speed visualization of refrigerant flows in 100×100 μm2 silicon multi-microchannels, Int. J. Refrig. 36 (2013) 402–413.

[26] C. Falsetti, H. Jafarpoorchekab, M. Magnini, N. Borhani, J.R. Thome, Two-phase operational maps, pressure drop, and heat transfer for flow boiling of R236fa in a micro-pin fin evaporator, Int. J. Heat Mass Transf. 107 (2017) 805–819.

[27] T.A. Kingston, J.A. Weibel, S.V. Garimella, An experimental method for controlled generation and characterization of microchannel slug flow boiling, Int. J. Heat Mass Transf. 106 (2017) 619–628.

[28] T. Harirchian, S.V. Garimella, The critical role of channel cross-sectional area in microchannel flow boiling heat transfer, Int. J. Multiph. Flow. 35 (2009) 904–913.

[29] C. Woodcock, X. Yu, J. Plawsky, Y. Peles, Piranha Pin Fin (PPF) — Advanced flow boiling microstructures with low surface tension dielectric fluids, Int. J. Heat Mass Transf. 90 (2015) 591–604.

[30] S.N. Ritchey, J.A. Weibel, S.V. Garimella, Effects of non-uniform heating on the location and magnitude of critical heat flux in a microchannel heat sink, Int. J. Micro-Nano Scale Transp. 5 (2014) 95–108.

[31] S.R. Rao, F. Houshmand, Y. Peles, Transient flow boiling heat-transfer measurements in microdomains, Int. J. Heat Mass Transf. 76 (2014) 317–329.

[32] S. Bigham, S. Moghaddam, Microscale study of mechanisms of heat transfer during flow boiling in a microchannel, Int. J. Heat Mass Transf. 88 (2015) 111–121.

[33] E. Cetegen, Force Fed Microchannel High Heat Flux Cooling Utilizing Microgrooved Surfaces, PhD Thesis, University of Maryland, 2010.

[34] D.C. Deisenroth, A. Bar-Cohen, M. Ohadi, Geometry effects on two-phase flow regimes in a diabatic manifolded microgap channel, in: International Technical Conference and Exhibition on Packaging and Integration of Electronic and Photonic Microsystems (2017) IPACK2017-74287.

[35] D.C. Deisenroth, A. Bar-Cohen, M. Ohadi, Heat transfer and two-phase flow regimes in manifolded microgaps - R245fa empirical results, in: Intersoc. Conf. Therm. Thermomechanical Phenom. Electron. Syst. (2019) 1168–1179.

[36] T. Brunschwiler, H. Rothuizen, M. Fabbri, U. Kloter, B. Michel, R.J. Bezama, G. Natarajan, Direct Liquid Jet-Impingment Cooling With Micron-Sized Nozzle Array and Distributed Return Architecture, in: Intersoc. Conf. Therm. Thermomechanical Phenom. Electron. Syst. (2006) 196–203.